

# Buoyancy statistics in moist turbulent Rayleigh–Bénard convection

JÖRG SCHUMACHER<sup>1</sup>† AND OLIVIER PAULUIS<sup>2</sup>

<sup>1</sup>Institut für Thermo- und Fluidodynamik, Technische Universität Ilmenau, Postfach 100565,  
D-98684 Ilmenau, Germany

<sup>2</sup>Courant Institute of Mathematical Sciences, New York University, 251 Mercer Street, New York,  
NY 10012-1185, USA

(Received 2 October 2009; revised 28 December 2009; accepted 28 December 2009)

We study shallow moist Rayleigh–Bénard convection in the Boussinesq approximation in three-dimensional direct numerical simulations. The thermodynamics of phase changes is approximated by a piecewise linear equation of state close to the phase boundary. The impact of phase changes on the turbulent fluctuations and the transfer of buoyancy through the layer is discussed as a function of the Rayleigh number and the ability to form liquid water. The enhanced buoyancy flux due to phase changes is compared with dry convection reference cases and related to the cloud cover in the convection layer. This study indicates that the moist Rayleigh–Bénard problem offers a practical framework for the development and evaluation of parameterizations for atmospheric convection.

---

## 1. Introduction

Moist thermal convection combines turbulent convection with phase changes and latent heat release. It is ubiquitous throughout the atmosphere of the Earth (Heintzenberg & Charlson 2009). When a parcel of air rises in convective motion, it expands adiabatically. As a consequence, its temperature and pressure drop and at some point during its ascent the air parcel becomes saturated. Once water condenses, a cloud is formed. The range of spatial and temporal scales in the convective turbulent motion varies widely, from a few hundred metres in isolated cumulus clouds to several thousands of kilometres in midlatitudes storm systems.

Despite its enormous importance, the small-scale structure and statistics of moist convective turbulence has been studied relatively little compared to its dry convection counterpart. The reason for this gap is that turbulent convection in moist air includes the complex nonlinear thermodynamics of phase changes in addition to the turbulent motion (Stevens 2005; Pauluis 2008). The associated latent heat release provides a rapidly changing local source of buoyant motion, so that moist convection is characterized by a complex interaction between dynamics and thermodynamics. One approach to this problem is to express the buoyancy of a parcel of moist air as function of its entropy, pressure and total water content. In such framework, phase changes can be treated implicitly and lead to discontinuities of the partial derivatives in the equation of state at the saturation point (Emanuel 1994). While moist convection remains poorly understood, significant progress has been made in the last decade

† Email address for correspondence: joerg.schumacher@tu-ilmenau.de

in understanding the global and local mechanisms of turbulent heat transfer in dry convection (for a comprehensive review see Ahlers, Grossmann & Lohse 2009). In this work, we aim at transferring some of the numerical analysis concepts from the well-investigated dry convection case, such as studies of the Rayleigh number dependence of the heat transfer (Verzicco & Camussi 2003), the flow properties in the cell (van Reeuwijk, Jonker & Hanjalić 2008) or the small-scale statistics (Emran & Schumacher 2008) to the less-explored moist convection case.

We propose here to take a first step by considering moist convection in the idealized setting of moist Rayleigh–Bénard convection with a linearized thermodynamics of phase changes (Pauluis & Schumacher 2010). On the one hand, the model is a straightforward extension of numerical studies in dry Rayleigh–Bénard convection in the Boussinesq approximation (e.g. Schumacher 2009). On the other hand, it is a generalization of a moist convection model that was discussed by Bretherton (1987, 1988) for the linear and weakly nonlinear regimes and has not been studied ever since. Here, we conduct direct numerical simulations (DNS) of the turbulent nonlinear stage of moist convection. This work reports systematic parameter investigations to understand the effect of phase change on the turbulent transport of buoyancy through the shallow layer. We also discuss the dependence of the cloud cover on the physical parameters of the model.

## 2. Moist Boussinesq model

The buoyancy  $B$  in atmospheric convection is given by (Emanuel 1994)

$$B(S, q_v, q_l, q_i, p) = -g \frac{\rho(S, q_v, q_l, q_i, p) - \bar{\rho}}{\bar{\rho}}, \quad (2.1)$$

where  $g$  is the gravity acceleration,  $\bar{\rho}$  is a mean density,  $p$  is the pressure,  $S$  is the entropy and  $q_v$ ,  $q_l$ ,  $q_i$  are the mixing ratios of water vapour, liquid water and ice, respectively. In the following, we discuss in brief the sequence of simplifications of the equation of state that result in a model of shallow non-precipitating moist convection in the Boussinesq approximation – the simplest case that goes beyond the well-known dry convection (Pauluis & Schumacher 2010). First, in the Boussinesq approximation the pressure variations about a mean hydrostatic profile are omitted when computing the buoyancy (Pauluis 2008) and one is left with  $B(S, q_v, q_l, q_i, z)$ . Second, warm clouds are discussed with  $q_i = 0$ . Third, we assume that the air parcels are in local thermodynamic equilibrium, which means that water vapour and condensed water can only co-exist at saturation line. This implies that liquid water is formed whenever a relative humidity of 100 % is exceeded. Furthermore, no rain can fall out in our model. The two remaining mixing ratios are then combined to the total water mixing ratio,  $q_T = q_v + q_l$ . This assumption also excludes the possibility of supersaturation. Condensation in the Earth’s atmosphere occurs primarily through heterogenous nucleation caused by a large number of cloud condensation nuclei ( $n \sim 10^9 \text{ m}^{-3}$ ). As a consequence, supersaturation rarely exceeds 1 % (Rogers & Yau 1989). In the absence of condensation nuclei in the fluid, homogeneous condensation may result in much larger supersaturation, as in a recent experiment by Zhong, Funkschilling & Ahlers (2009), where the condensate is formed at the top plate of the convection cell. The assumption of local thermodynamic equilibrium has the practical advantage that, once the entropy and pressure are known, the total water content can be separated between the vapour and liquid phases. The dependencies of the buoyancy are thus reduced to  $B(S, q_T, z)$ . The buoyancy is still a highly nonlinear

function of the entropy, total water mixing ratio and height. Fourth, we approximate  $B$  as a piecewise linear function of the two state variables  $S$ ,  $q_T$  at each height  $z$  around the phase boundary between gas and liquid. The linearization step restricts us to a shallow layer since the height variations of thermodynamic quantities have to remain small. It preserves the main physical ingredient: the discontinuity of partial derivatives (e.g. the specific heat) at the phase boundary. It also allows for an explicit determination of whether an air parcel is saturated or not. Finally, since  $B$  is a linear function of  $S$  and  $q_T$ , we can introduce two new prognostic buoyancy fields: a ‘dry buoyancy field’  $D$  (which corresponds to a liquid water potential temperature) and a ‘moist buoyancy field’  $M$  (which corresponds to an equivalent potential temperature). They are linear combinations of  $S$  and  $q_T$ . Since the state variables  $S$  and  $q_T$  are adiabatic invariants, the two new state variables  $M$  and  $D$  are also conserved by adiabatic transformations. Consequently, the original buoyancy  $B(S, q_v, q_l, q_i, p)$  is simplified to  $B(M, D, z)$ , a linear function of the fields  $M$  and  $D$  which is given by

$$B(\mathbf{x}, t) = \max (M(\mathbf{x}, t), D(\mathbf{x}, t) - N_s^2 z), \quad (2.2)$$

where  $N_s$  is the Brunt–Väisälä frequency. This is the saturation condition in our model.

The dry and moist buoyancy fields can be decomposed in

$$D(\mathbf{x}, t) = \bar{D}(z) + D'(\mathbf{x}, t) = D_0 + \frac{D_H - D_0}{H} z + D'(\mathbf{x}, t), \quad (2.3)$$

$$M(\mathbf{x}, t) = \bar{M}(z) + M'(\mathbf{x}, t) = M_0 + \frac{M_H - M_0}{H} z + M'(\mathbf{x}, t). \quad (2.4)$$

The variations about the mean linear profiles of both fields have to vanish at  $z = 0$  and  $H$ . Equation (2.2) can now be transformed into

$$B = \bar{M}(z) + \max (M', D' + \bar{D}(z) - \bar{M}(z) - N_s^2 z). \quad (2.5)$$

Note that the first term on the right-hand side is horizontally uniform. This implies that it can be balanced by a horizontally uniform pressure field given by  $p(z) = -M_0 z - [(M_H - M_0)/(2H)]z^2$ . We can thus remove the mean contribution from the buoyancy field without any loss of generality. A dimensionless version of the equations of motion is obtained by defining the characteristic quantities. These are the height of the layer  $H$ , the free-fall velocity  $U_f = \sqrt{H(M_0 - M_H)}$ , the time  $T_f = H/U_f$ , the characteristic pressure  $U_f^2$  and the buoyancy difference  $M_0 - M_H$ . The equations, together with the decompositions (2.3) and (2.4), are given by

$$\frac{\partial \mathbf{u}}{\partial t} + (\mathbf{u} \cdot \nabla) \mathbf{u} = -\nabla p + \sqrt{\frac{Pr}{Ra_M}} \nabla^2 \mathbf{u} + B(M, D, z) \mathbf{e}_z, \quad (2.6)$$

$$\nabla \cdot \mathbf{u} = 0, \quad (2.7)$$

$$\frac{\partial D'}{\partial t} + (\mathbf{u} \cdot \nabla) D' = \frac{1}{\sqrt{Pr Ra_M}} \nabla^2 D' + \frac{Ra_D}{Ra_M} u_z, \quad (2.8)$$

$$\frac{\partial M'}{\partial t} + (\mathbf{u} \cdot \nabla) M' = \frac{1}{\sqrt{Pr Ra_M}} \nabla^2 M' + u_z. \quad (2.9)$$

These equations contain three non-dimensional parameters, the Prandtl number  $Pr$ , the dry and the moist Rayleigh numbers  $Ra_D$  and  $Ra_M$

$$Pr = \frac{\nu}{\kappa}, \quad Ra_D = \frac{H^3(D_0 - D_H)}{\nu \kappa}, \quad Ra_M = \frac{H^3(M_0 - M_H)}{\nu \kappa}. \quad (2.10)$$

Under most circumstances, the amount of water in the atmosphere decreases with height. This implies that the moist Rayleigh number should be larger than the dry Rayleigh number,  $Ra_M \geq Ra_D$ . In addition to the three parameters explicitly present in (2.6)–(2.9), two more parameters are hidden implicitly within the definition (2.5) of the buoyancy  $B$ , which is given in dimensionless form by

$$B = \max \left( M', D' + SSD + \left( 1 - \frac{Ra_D}{Ra_M} \right) z - CSAz \right). \quad (2.11)$$

The so-called surface saturation deficit ( $SSD$ ) and the condensation in saturated ascent ( $CSA$ ) are then defined as

$$SSD = \frac{D_0 - M_0}{M_0 - M_H} \quad \text{and} \quad CSA = \frac{N_s^2 H}{M_0 - M_H}. \quad (2.12)$$

These two new non-dimensional parameters respectively measure how close the lower boundary is to saturation and how much water can condense within the atmospheric layer during an adiabatic ascent of a saturated air parcel. The larger  $CSA$ , the easier is the formation of liquid water and thus of clouds. When  $D_0 - M_0$  is positive, the air at the lower boundary is unsaturated, and  $D_0 - M_0$  is proportional to the ‘water deficit’, i.e. the amount of water vapour that must be added to the air parcel to become saturated. A positive  $SSD$  would occur over the continents. For convection over the ocean, the lower boundary is neither saturated nor unsaturated, i.e.  $SSD = 0$ . It is clear that we can consider a subspace of the five-dimensional parameter space only which is spanned in general by  $Ra_D, Ra_M, Pr, SSD$  and  $CSA$ . Therefore, this study is restricted to  $Pr = 0.7$  and  $SSD = 0$ . The variation of  $SSD$  while keeping the other parameters fixed was discussed by Pauluis & Schumacher (2010).

The equations of motion are solved by a pseudospectral scheme with volumetric fast Fourier transformations and 2/3 de-aliasing in a Cartesian slab with side lengths  $\Gamma H \times \Gamma H \times H$ . Here  $\Gamma$  is the aspect ratio of the slab. In lateral directions  $x$  and  $y$ , we apply periodic boundary conditions. In the vertical  $z$  direction, we apply free-slip boundary conditions

$$u_z = D' = M' = 0 \quad \text{and} \quad \frac{\partial u_x}{\partial z} = \frac{\partial u_y}{\partial z} = 0. \quad (2.13)$$

The boundary conditions, which have also been used by Bretherton (1987, 1988), approximate a situation over an ocean surface at the bottom and a temperature inversion at the top. Time stepping is done by a second-order Runge–Kutta scheme. Since both buoyancy fields are linearly unstable, the requirements on mesh resolution and time stepping are the same as in dry convection. The additional scalar field and the update of the  $B$  increases computational costs by 20%. Table 1 summarizes the grid resolutions and dimensionless parameter sets that are taken in the direct numerical simulations. The spectral resolution does not go below  $k_{max} \eta_K = 2.45$  for all DNS, where  $k_{max}$  is the maximum resolved wavenumber and  $\eta_K$  is the Kolmogorov length. Technically, we use  $B'$  in the momentum equation (2.6) instead of  $B$  since the mean contribution is  $\overline{B}(z)$  which can be added to the kinematic pressure, i.e.  $\partial_z p + B = \partial_z \tilde{p} + B'$ . For the moist runs, we distinguish two classes for initial equilibrium configurations – a fully saturated slab which corresponds with  $\overline{M}(z) > \overline{D}(z) - N_s^2 z$  (large  $CSA$ ) and a fully unsaturated slab with  $\overline{M}(z) < \overline{D}(z) - N_s^2 z$  (small  $CSA$ ).

Run	$N_x \times N_y \times N_z$	$Ra_M$	$Ra_D$	CSA	$U_f$	$T_f$	$T/T_f$	$\frac{u_{rms}}{U_f}$	$\frac{M_{rms}}{M_0 - M_H}$
1*	$512 \times 512 \times 65$	$9.5 \times 10^5$	$7.0 \times 10^5$	0.53	3.06	1.03	141	0.356	0.434
2*	$512 \times 512 \times 65$	$1.1 \times 10^6$	$7.0 \times 10^5$	0.44	3.35	0.94	154	0.334	0.436
3	$512 \times 512 \times 65$	$1.4 \times 10^6$	$7.0 \times 10^5$	0.35	3.75	0.84	173	0.272	0.432
4	$512 \times 512 \times 65$	$1.9 \times 10^6$	$7.0 \times 10^5$	0.26	4.36	0.72	368	0.225	0.431
5	$512 \times 512 \times 65$	$2.9 \times 10^6$	$7.0 \times 10^5$	0.17	5.35	0.59	449	0.184	0.433
6	$512 \times 512 \times 65$	–	$7.0 \times 10^5$	0.00	2.63	1.19	122	0.362	–
7*	$1024 \times 1024 \times 129$	$9.5 \times 10^6$	$7.0 \times 10^6$	0.53	3.06	1.03	342	0.308	0.436
8*	$1024 \times 1024 \times 129$	$1.1 \times 10^7$	$7.0 \times 10^6$	0.44	3.35	0.94	407	0.287	0.437
9	$1024 \times 1024 \times 129$	$1.4 \times 10^7$	$7.0 \times 10^6$	0.35	3.75	0.84	412	0.240	0.436
10	$1024 \times 1024 \times 129$	$1.9 \times 10^7$	$7.0 \times 10^6$	0.26	4.36	0.72	431	0.194	0.434
11	$1024 \times 1024 \times 129$	$2.9 \times 10^7$	$7.0 \times 10^6$	0.17	5.35	0.59	587	0.158	0.436
12	$1024 \times 1024 \times 129$	–	$7.0 \times 10^6$	0.00	2.63	1.19	321	0.320	–
13*	$2048 \times 2048 \times 257$	$1.1 \times 10^8$	$7.0 \times 10^7$	0.44	3.35	0.94	125	0.258	0.439
14	$2048 \times 2048 \times 257$	$1.9 \times 10^8$	$7.0 \times 10^7$	0.26	4.36	0.72	150	0.176	0.438

TABLE 1. Parameters of simulation runs: grid resolution,  $Ra_M$ ,  $Ra_D$  and CSA. For all runs,  $Pr = 0.7$ ,  $\Gamma = 8$  and  $SSD = 0$ . We also display the characteristic velocity  $U_f = \sqrt{(M_0 - M_H)H}$ , the characteristic time scale  $T_f = H/U_f$  and the total integration time  $T/T_f$ . For dry runs 6 and 12,  $U_f = \sqrt{(D_0 - D_H)H}$ . Furthermore,  $u_{rms}/U_f$  with  $u_{rms} = \sqrt{\langle u_x^2 + u_y^2 + u_z^2 \rangle_{x,y,z,t}}$  and  $M_{rms}/(M_0 - M_H)$  with  $M_{rms} = \sqrt{\langle M'^2 \rangle_{x,y,z,t}}$  are shown. Runs that are labelled with an asterisk start out of a completely saturated equilibrium,  $\overline{M}(z) > \overline{D}(z) - N_s^2 z$ .

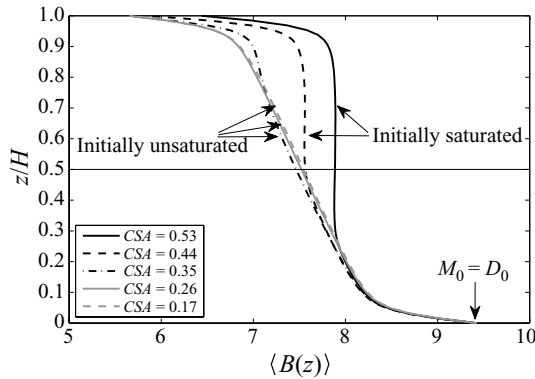


FIGURE 1. Mean total buoyancy profiles  $\langle B(z) \rangle$  for runs 1–5. All runs have the same amplitude of  $M_0$  (which equals  $D_0$ ). It is also indicated for which runs the initial equilibrium solution is completely unsaturated or saturated. Profiles for the series with  $Ra_D = 7 \times 10^6$  look qualitatively similar, except that the boundary-layer thickness decreased.

### 3. Results

#### 3.1. Buoyancy and velocity fluctuations

Initially, the equilibrium configuration is perturbed infinitesimally and after  $T/T_f \sim 10^2$  the flow is relaxed into a fully developed and statistically stationary turbulent state. This is when the statistical analysis is started. As indicated in the table, we restrict dependencies of moist convection on the two Rayleigh numbers and parameter CSA. Figure 1 shows the mean vertical profile of the buoyancy,

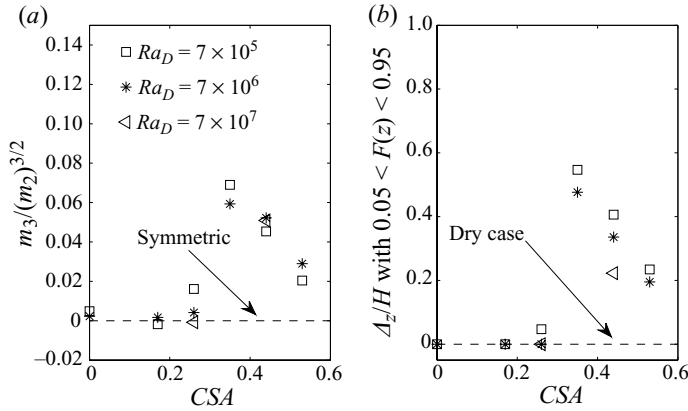


FIGURE 2. Asymmetry of the velocity fluctuations as a function of  $CSA$  and  $Ra_D$ . (a) Skewness  $m_3/m_2^{3/2}$  of the vertical profiles of the r.m.s. of the vertical velocity component  $u_z$ . (b) Vertical fraction  $\Delta z/H$  of the layer with  $0.05 < F(z) < 0.95$ , where  $F(z)$  is given by (3.5).

$\langle B(z) \rangle$ , which is obtained by taking averages in the  $z$  planes and over an ensemble of statistically independent snapshots. It is observed that this profile becomes strongly asymmetric for the cases that started with an initially fully saturated equilibrium. These will be the cases where phase changes affect the turbulence properties most strongly.

Table 1 lists the root-mean-square (r.m.s.) values of  $M$  and  $\mathbf{u}$  as obtained in the statistically stationary regime. Since both buoyancy fields follow a linear advection–diffusion equation, the ratio of the r.m.s. fluctuations to the outer buoyancy difference  $M_0 - M_H$  should be constant. The velocity r.m.s. fluctuations decrease with decreasing  $CSA$ . At fixed  $CSA$ , the fluctuations decrease also with increasing Rayleigh number  $Ra_D$ . This result is also observed in dry convection (Verzicco & Camussi 2003). In figure 2, we refine this analysis and study the vertical profile of the r.m.s. of the vertical velocity component,  $u_{z,rms}(z) = \sqrt{\langle u_z^2(z) \rangle_{x,y,t}}$ . A measure of asymmetry of the profile with respect to the midplane  $z = H/2$  can be based on the moments  $m_n = \int_0^H (z - (H/2))^n u_{z,rms}(z) dz$ . If the skewness  $m_3/m_2^{3/2}$  is larger than zero then the vertical velocity fluctuations are enhanced in the upper half of the slab. Figure 2(a) shows that the profile is symmetric for the dry reference run and those with smaller amount of water which can be condensed. Asymmetry is observed for  $CSA \geq 0.35$ , which peaks at  $CSA = 0.35$  and decreases again for larger  $CSA$ . We will show at the end of § 3.2 that the asymmetry in the vertical velocity fluctuations is directly coupled to the vertical fraction  $\Delta z/H$  of the convection layer that is partially saturated and unsaturated. This fraction turns out to be largest at  $CSA = 0.35$  for all  $Ra_D$  (see figure 2b). It is also found that isotropy in the velocity fluctuations is established to a better degree with increasing  $Ra_D$ . We conclude that phase changes cause the asymmetry of the vertical velocity fluctuations. However, with increasing Rayleigh number and thus Reynolds number, the small-scale turbulence is found at increasingly isotropic conditions which can compensate this trend in parts.

Of central importance in dry convection is the one-point-correlation between buoyancy (or temperature) and vertical velocity,  $\langle u_z B(z) \rangle$  (which is equal to  $\langle u_z B'(z) \rangle$ ). It enters the definition of the dimensionless measure of buoyancy flux through the layer, the Nusselt number  $Nu$ . In the present model, we can define two Nusselt

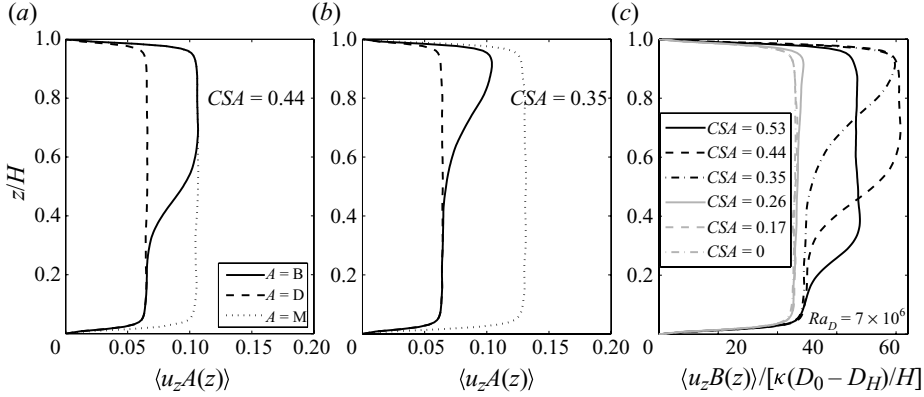


FIGURE 3. Convective part of the buoyancy flux as a function of  $Ra_D$ ,  $Ra_M$  and  $CSA$ . (a) Relation between the fluxes  $\langle u_z D(z) \rangle$ ,  $\langle u_z M(z) \rangle$  and  $\langle u_z B(z) \rangle$ . Data are for  $CSA = 0.44$  and  $Ra_D = 7.0 \times 10^6$ . (b) The same as (a) for  $CSA = 0.35$ . (c)  $\langle u_z B(z) \rangle$  normalized by the corresponding dry diffusive buoyancy flux which is given as  $\kappa(D_0 - D_H)/H$ . Data are for runs 7–12.

numbers for both fields in a standard way, such as  $Nu_D(z) = [\langle u_z D(z) \rangle - \kappa \partial_z \langle D(z) \rangle] / [\kappa(D_0 - D_H)/H]$  for  $D$  which is constant and thus simply denoted by  $Nu_D$ . Since  $Nu_D$  and  $Nu_M$  are normalized with respect to their diffusive fluxes,  $Nu_D = Nu_M$  follows which was verified in the simulations. In order to quantify the additional amount of buoyancy transfer, we will relate the correlations  $\langle u_z B(z) \rangle$  to the dry field in the following. Note that the buoyancy flux  $\langle u_z B(z) \rangle$  is tied to the correlations  $\langle u_z D(z) \rangle$  and  $\langle u_z M(z) \rangle$ . Moreover, because the partial derivative of the buoyancy with respect to  $M$  and  $D$  is bound by 0 and 1 (see (2.2)), we have automatically that at each level  $z$

$$\langle u_z D(z) \rangle \leq \langle u_z B(z) \rangle \leq \langle u_z M(z) \rangle. \quad (3.1)$$

The lower bound ( $\langle u_z D(z) \rangle = \langle u_z B(z) \rangle$ ) occurs when a layer is fully unsaturated, while the upper bound ( $\langle u_z B(z) \rangle = \langle u_z M(z) \rangle$ ) is achieved in a fully saturated layer. This is demonstrated in figures 3(a) and 3(b). In figure 3(c), we normalize the correlation by the dry diffusive buoyancy flux (which would correspond with  $Nu_D = 1$ ). It is given by  $\kappa(D_0 - D_H)/H$ . Again, we observe an enhancement of the correlations for the three largest values of  $CSA$ . The profiles for the two smaller values of  $CSA$  collapse almost perfectly with the corresponding dry reference cases in both series of DNS. Note that a normalization by the moist diffusive buoyancy flux  $\kappa(M_0 - M_H)/H$  would result in systematic growth of the correlation since an increase of  $Ra_M$  is in line with a decrease of  $CSA$ . Finally, the correlations increase as well when the Rayleigh numbers  $Ra_D$  and  $Ra_M$  are enhanced at given  $CSA$ .

On the basis of the correlations between buoyancy and vertical velocity and the mean vertical profiles, the additional buoyancy flux due to phase changes can be determined. We define a Nusselt number based on the dry diffusive buoyancy flux:

$$Nu_B(z) = \frac{\langle u_z B(z) \rangle - \kappa \partial_z \langle B(z) \rangle}{\kappa(D_0 - D_H)/H}, \quad (3.2)$$

which is not necessarily constant with height, as can be seen in figure 4. A similar behaviour was found by Oresta *et al.* (2009) in bubbly convection with phase changes. The additional buoyancy flux due to phase changes and latent heat release can be

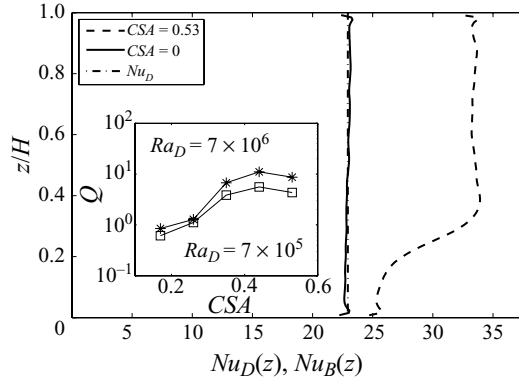


FIGURE 4. Vertical profiles of  $Nu_D(z)$  and  $Nu_B(z)$  as given by (3.2). Data are for runs 7 and 12. The additional amount of buoyancy,  $Q$  is the area between moist and dry reference profiles. The inset shows  $Q$  as a function of  $CSA$  and  $Ra_D$  (runs 1–5 and 7–11).

quantified in terms of the parameter:

$$Q = \frac{1}{H} \int_0^H Nu_B(z) dz - Nu_D. \quad (3.3)$$

The upper and lower bounds on the buoyancy flux (3.1) imply that the enhancement factor  $Q$  is itself bound by  $1 \leq Q \leq Ra_M/Ra_D$ . Figure 4 shows  $Q$  as a function of  $CSA$  and  $Ra_D$ . The sensitivity of  $Q$  to  $CSA$  at a given value of  $Ra_D$  is complex. On the one hand, a high value of  $CSA$  implies more water and a deeper saturated layer. On the other hand, in our experimental set-up with  $SSD = 0$  and constant  $Ra_D$ , any increase of  $CSA$  is connected with a decrease of  $Ra_M$ . We observe here a maximum of  $Q$  at  $CSA = 0.44$ . This is the case where in figure 3 the largest amplitudes for  $\langle u_z B(z) \rangle$  are observed (see the dashed line in figure 3c).

### 3.2. Cloud cover

The phase changes in the convective turbulence are associated with the appearance and disappearance of clouds. They are defined as sites where the liquid water mixing ratio  $q_l(\mathbf{x}, t) > 0$ . Translated into our framework, this corresponds with

$$q_l(\mathbf{x}, t) = M(\mathbf{x}, t) - [D(\mathbf{x}, t) - N_s^2 z] > 0. \quad (3.4)$$

The cloud boundary is given by  $q_l = M - D + N_s^2 z = 0$ . Depending on  $CSA$  and both Rayleigh numbers, this is a simply connected isosurface or a collection of disconnected isosurfaces. The latter case is illustrated in figure 5. The white isosurfaces  $q_l = 0$  display isolated clouds. They are correlated with strong updrafts as illustrated by the red isosurfaces for  $u_z \geq 0.23U_f$ . Warm air rises up and expands adiabatically such that the temperature decreases and condensation sets in.

Figures 6(a) and 6(b) display the probability to find clouds at height  $z$  in the slab as a function of  $Ra_D$  and  $CSA$  in a semi-logarithmic plot. The formation of clouds is less probable when  $Ra_D$  is increased. Reasons could be the stronger filamentation of the turbulent patches and the decreased velocity fluctuations which are in line with an increase of the Reynolds number of the turbulent flow. For  $CSA = 0.53$  and  $0.44$ , the cloud layer is closed for all  $Ra_D$ , which is in line with  $P(z|q_l \geq 0) = 1$ . For  $CSA = 0.35, 0.26$  and  $0.17$ , a broken cloud layer with isolated clouds can be observed.

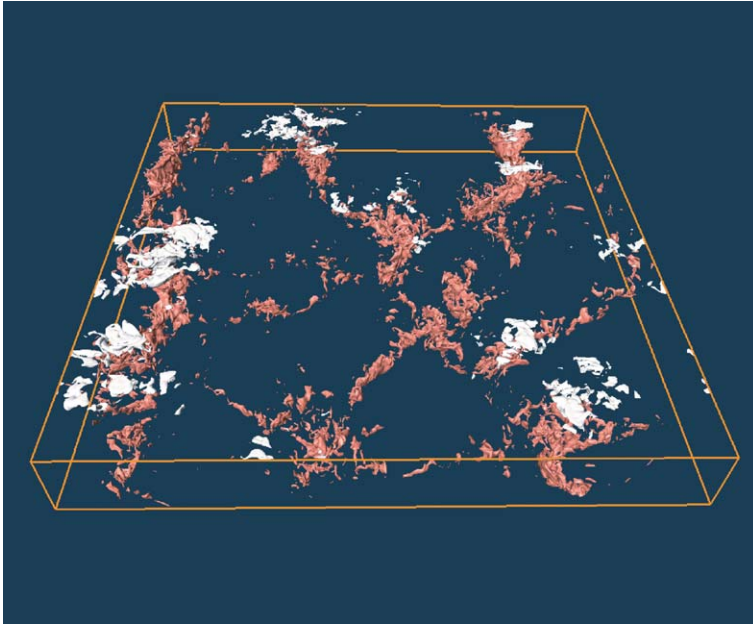


FIGURE 5. Snapshot of the instantaneous cloud distribution (white isosurface) in combination with the updrafts (red isosurface). The white isosurface is the cloud boundary with  $q_l = 0$ . The red isosurface is for  $u_z \geq 0.23U_f$  or  $1.5u_{rms}$ . Data are for run 14 with  $CSA = 0.26$ .

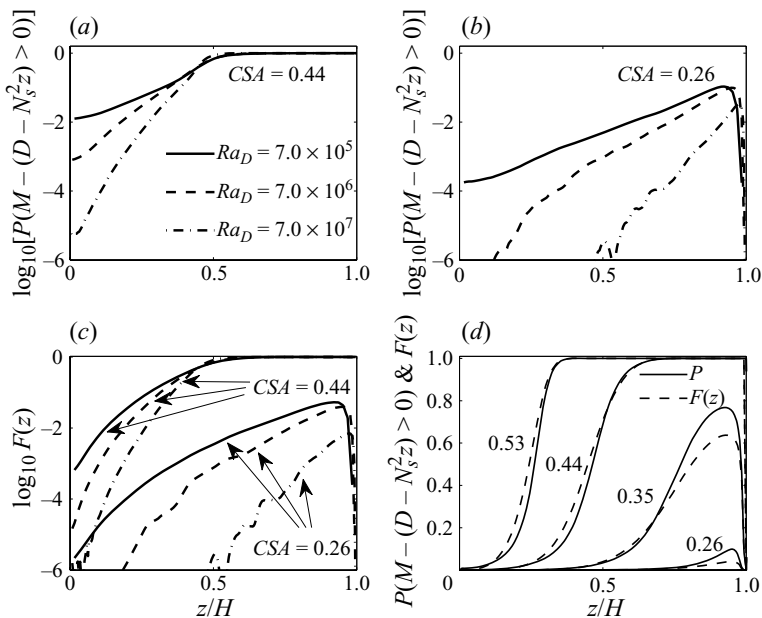


FIGURE 6. Measures of the cloud cover. (a) Probability  $P$  to find clouds in a layer at height  $z$  as a function of  $Ra_D$ . Data are for  $CSA = 0.44$ . (b) The same as in (a) for  $CSA = 0.26$ . The corresponding dry Rayleigh numbers for both (a and b) are given in (a). (c) Function  $F(z)$  as a function of  $Ra_D$  and  $CSA$ . Line styles correspond with (a). (d) Comparison of  $P$  and  $F(z)$  for runs 1–5. Data for run 5 at  $CSA = 0.17$  coincide with the axis.

While the former could correspond with a stratocumulus-like convection regime, the latter could correspond with a cumulus-like regime. Note also that layer remains basically dry for the smallest *CSA*.

The presence of clouds is also related to the enhancement of the buoyancy flux. We define a saturation fraction  $F(z)$  for the buoyancy flux that follows from (3.1) and is given by

$$F(z) = \frac{\langle u_z B(z) \rangle - \langle u_z D(z) \rangle}{\langle u_z M(z) \rangle - \langle u_z D(z) \rangle}. \quad (3.5)$$

This saturation fraction is such that in a fully saturated environment  $F(z) = 1$ , while in an unsaturated environment, we have  $F(z) = 0$ . Figures 6(c) and 6(d) replot the same data sets for  $F(z)$  and in figure 6(d) a direct comparison with  $P(z|q_l \geq 0)$  is provided. On the basis of the data, we can conclude that both measures collapse quite well for a fully saturated or unsaturated layer, but the case  $CSA = 0.35$  indicates there are some significant departures in partially saturated layers. Finally, one can define now the vertical fraction of the layer that is partially saturated and unsaturated as  $0.05 < F(z) < 0.95$  (see figure 6d). This fraction is biggest for the runs at  $CSA = 0.35$  as shown in figure 3(b). In this case, the asymmetry between saturated ascents and unsaturated descents can be expected to be largest. Consequently, the largest asymmetries of the vertical velocity fluctuations can be built up. The peak at exactly the same *CSA* value in figure 3(a, b) supports our conclusion and closes the loop between buoyancy transfer, cloud cover and vertical flow asymmetry.

#### 4. Summary and conclusions

We have presented a shallow moist convection model with a linear equation of state for the thermodynamics of phase changes. This model that contains five dimensionless parameters is discussed in a three-dimensional subspace due to fixed Prandtl number and *SSD*. The most important simplification that reduces the complexity is the assumption of a local thermodynamic equilibrium. Several key physical processes, such as the formation of precipitation and the existence of supersaturation, are thus omitted. The model nevertheless captures the fundamental interactions between phase transition and dynamics. Phase changes cause an asymmetry of the vertical velocity fluctuations when the amount of water that can be condensed (parameter *CSA*) is sufficiently large. Similar to the dry convection case, the correlations between vertical velocity and buoyancy are used to quantify the amount of additional buoyancy flux due to condensation and related latent heat release. Furthermore, this correlation can be connected with the cloud cover in the layer.

The studies in this simplified setting provide thus a basis for possible parameterizations of cloud impact in large-scale models. In particular, determining the factors that control cloud fraction is a central issue in climate modelling, as small changes in cloud cover can dramatically affect the amount of energy received and emitted by the atmosphere. We found here that the Rayleigh number has a direct impact on the cloud cover, which should be a cause of concern, as the Rayleigh number in our numerical simulations ( $Ra_D = 7 \times 10^7$ ) is significantly smaller than its typical atmospheric value,  $Ra \approx 10^{18} - 10^{22}$ . Nevertheless, the idealized moist Rayleigh–Bénard convection provides an important test for our understanding of clouds and their sensitivity to environmental parameters.

We thank the DEISA Consortium ([www.deisa.eu](http://www.deisa.eu)), co-funded through the EU FP6 project RI-031513 and the FP7 project RI-222919, for support within the DEISA Extreme Computing Initiative. J.S. is supported by DFG grants SCHU 1410/9-1 and SCHU 1410/5-1 and O.P. by NSF grant ATM-0545047.

#### REFERENCES

- AHLERS, G., GROSSMANN, S. & LOHSE, D. 2009 Heat transfer and large-scale dynamics in turbulent Rayleigh–Bénard convection. *Rev. Mod. Phys.* **81**, 503–537.
- BRETHERTON, C. S. 1987 A theory for nonprecipitating moist convection between two parallel plates. Part I. Thermodynamics and ‘linear’ solutions. *J. Atmos. Sci.* **44**, 1809–1827.
- BRETHERTON, C. S. 1988 A theory for nonprecipitating moist convection between two parallel plates. Part II. Nonlinear theory and cloud field organization. *J. Atmos. Sci.* **45**, 2391–2415.
- EMANUEL, K. A. 1994 *Atmospheric Convection*. Oxford University Press.
- EMRAN, M. S. & SCHUMACHER, J. 2008 Fine-scale statistics of temperature and its derivatives in convective turbulence. *J. Fluid Mech.* **611**, 13–34.
- HEINTZENBERG, J. & CHARLSON, R. J. 2009 *Clouds in the Perturbed Climate System*. MIT Press.
- ORESTA, P., VERZICCO, R., LOHSE, D. & PROSPERETTI, A. 2009 Heat transfer mechanisms in bubbly Rayleigh–Bénard convection. *Phys. Rev. E* **80**, 026304.
- PAULUIS, O. 2008 Thermodynamic consistency of the anelastic approximation for a moist atmosphere. *J. Atmos. Sci.* **65**, 2719–2729.
- PAULUIS, O. & SCHUMACHER, J. 2010 Idealized moist Rayleigh–Bénard convection with piecewise linear equation of state. *Commun. Math. Sci.* **8**, 295–319.
- VAN REEUWIJK, M., JONKER, H. J. J. & HANJALIĆ, K. 2008 Wind and boundary layers in Rayleigh–Bénard convection. Part I. Analysis and modelling. *Phys. Rev. E* **77**, 036311.
- ROGERS, R. R. & YAU, M. K. 1989 *A Short Course in Cloud Physics*, 3rd edn. Butterworth-Heinemann.
- SCHUMACHER, J. 2009 Lagrangian studies in convective turbulence. *Phys. Rev. E* **79**, 056301.
- STEVENS, B. 2005 Moist convection. *Annu. Rev. Earth Planet. Sci.* **33**, 605–643.
- VERZICCO, R. & CAMUSSI, R. 2003 Numerical experiments on strongly turbulent thermal convection in a slender cylindrical cell. *J. Fluid Mech.* **477**, 19–49.
- ZHONG, J.-Q., FUNFSCHILLING, D. & AHLERS, G. 2009 Enhanced heat transport by turbulent two-phase Rayleigh–Bénard convection. *Phys. Rev. Lett.* **102**, 124501.